Science Advances
AAAS

Supplementary Materials for

Effects of rare-earth magnetism on the superconducting upper critical field in infinite-layer nickelates

Bai Yang Wang *et al.*

Corresponding author: Bai Yang Wang, bwang87@stanford.edu; Tiffany C. Wang, catwang@stanford.edu; Harold Y. Hwang, hyhwang@stanford.edu

Sci. Adv. **9**, eadf6655 (2023)
DOI: 10.1126/sciadv.adf6655

This PDF file includes:

Supplementary Text

High field magnetoresistance properties of additional La- and Pr- samples

We show the magnetoresistance for additional $La_{1-x}Sr_xNiO_2$, $Pr_{1-x}Sr_xNiO_2$, and $Nd_{1-x}Sr_xNiO_2$ (*20*) samples (fig. S1). Across Sr doping, both La- and Pr-nickelates require magnetic field up to 35 T (or beyond) to fully suppress superconductivity. In contrast, except for $x = 0.175$, a 20 T magnetic field is sufficient to bring the Nd-nickelates into the normal state. In addition, as Sr doping is increased, the field scales at which the superconductivity is destroyed converge between the two field orientations and eventually cross for $x = 0.225$.

Doping dependence of H_{c2} for all three nickelate variants

Here we show the H_{c2} data of Fig. 1F in a decompressed format to more clearly illustrate their doping dependences (fig. S2). For each variant, the bottom panel shows the corresponding superconducting dome traced out by the T_{c0} values of the four dopings investigated. For each doping, the corresponding $H_{c2\perp}$ and $H_{c2\parallel}$ are plotted in a pair of panels, marked by the black arrows. For all three nickelate variants and across all measured dopings, near T_{c0}, we consistently observe the linear temperature dependence for $H_{c2\perp}$ (top panel of each pair) and $(1-T/T_{c0})^{1/2}$ temperature dependence for $H_{c2\parallel}$ (bottom panel of each pair).

Angular magnetoresistance properties of additional samples

The reported anomalous angular magnetoresistance is seen in all 16 measured Nd-nickelate samples and absent in all 7 measured La- and Pr-nickelates. We show the temperature and field dependence of the angular magnetoresistance of additional representative nickelate samples of all three *R*-variants in figs. S3 to S5. While there are sample to sample variations, the overall angular

magnetoresistance behavior and doping evolution are qualitatively consistent and robust to details of the growth conditions. In particular, for the Nd-nickelates, the $x = 0.15$, $x = 0.2$ sample #2, and $x = 0.225$ sample #3 were grown using conditions reported in ref. *1,* and the rest were grown using the conditions reported in ref. *40*. Therefore, we attribute the deviations to sample quality differences. Thus while only two of the three $x = 0.225$ samples exhibit higher resistance at $\theta = 0$, the substantial impact of the EMP effect is evident in all three samples. The same fittings for the θ- and ϕ-dependence (Eqs. 1 and 2 of the main text) are shown as black dashed lines. In contrast, the La- and Pr-nickelates all follow the expected AOD dominant θ-dependence and the vortex-driven C_2 ϕ-dependence.

Vortex origin of anomalous angular magnetoresistance

Anomalous θ- and ϕ-dependent magnetoresistance features have been seen in cuprate superconductors, and attributed to the angular dependence of the vortex pinning mechanisms (*32, 33*). For θ-dependence, a symmetric pair of sharp resistance peaks is observed when the field orientation slightly deviates from the in-plane direction, which is a result of the introduction of mobile inter-layer segments of the vortices. In addition, a small resistance dip is observed for the $H_\perp$ orientation, which is due to vortices locking to vertical defects, such as domain or anti-phase boundaries (*32*). For ϕ-dependence, a two-fold symmetric magnetoresistance pattern is seen, since the Lorentz force acting on the vortices has a two-fold ϕ-dependence. Additionally, in $YBa_2Cu_3O_{7-x}$, a four-fold clover leaf pattern has been observed, which is attributed to the additional vortex pinning from orthorhombic domain boundaries (*32, 33*).

However, our observed anomalous angular magnetoresistance cannot be explained by vortex pinning mechanisms. First, previous observations in the cuprates are sensitive to the measurement current density and are only visible in the presence of large current density (~8E+5 A/cm^2, J_c ~5E+6 A/cm^2) (*50*) and small magnetic field (6 T relative to ~70 K T_{c0}) (*32*). In contrast, our observations are seen in small current density (~40 A/cm^2, J_c ~3E+5 A/cm^2) (*1, 2*) and large magnetic field (~H_{c2}). To examine this further, we studied the angular magnetoresistance dependence on measurement current. As shown in fig. S6, we vary the current density by up to 3 orders of magnitude and see no qualitative changes to either the θ- or ϕ-dependence. A further inconsistency with the previous cuprate observations is found in the angular position of the anomalous features in the θ-dependence. While they only occur near the principle axes in the cuprates, the angular modulations reported in this work occur predominantly between the principle axes. This is in contrast to the directional preference of the potential vortex pinning defects in Nd-nickelates, which are vertical Ruddlesden-Popper faults (favoring pinning along the *c*-axis) and precipitates concentrated at the film surface (with no clear directional preference for pinning). Considering these distinctions, we conclude that vortex dynamics are not the origin of our observations.

Crystal field calculations of rare-earth 4*f* moments

We investigate the crystal field splitting of the 4*f* levels through numerical calculations. We treat the static tetragonal crystal field as a perturbation Hamiltonian, described as:

$$H_{CEF} = B_2^0 O_2^0 + B_4^0 O_4^0 + B_6^0 O_6^0 + B_4^4 O_4^4 + B_6^4 O_6^4,$$

where B_n^ms are the crystal field parameters and O_n^ms are the Steven Operators. The five terms are the only non-zero terms given the tetragonal symmetry of the unit cell (*51*). While the

decomposition of Steven operators O are well tabulated, the crystal field parameters B_n^m are dependent on the exact distribution of the surrounding charge within the unit cell. For the B_n^m calculation, we adopt the point charge approximation, as we are primarily interested in the energy hierarchy of the split levels (*51*).

To obtain the electron density distributions, we implement density functional theory (DFT) calculations with Perdew-Burke-Ernzerhof (*35*) exchange-correlation functional using the Vienna *Ab initio* Simulation Package (VASP) (*36*). The pseudopotentials for Nd and Pr are taken as the Nd^{3+} and Pr^{3+} with the 4*f* electrons in the core. We calculate the electron density distributions associated with *R* 5*d* and 6*s* orbitals, O 2*p* orbitals and Ni 3*d* and 4*s* orbitals, totaling 33 electrons per unit cell (11 electrons for *R*, and 10 electrons for Ni and 6 electrons for each O in the pseudopotentials). Using Bader charge analysis (*37, 52*) we dissect the total electron density distribution into separate regions and assign each region to the corresponding ions. We also treat the positive ionic charges as point charges localized at each ionic site. Adding the two, we obtain the effective valence of Ni, O, and Nd to be: 0.7^+, 1.31^-, and 1.93^+, localized at each ionic site. Then B_n^m can be calculated (*51*) according to:

$$B_n^m = \left(\sum_i \frac{4\pi}{2n+1} q_i \frac{Z_{nm}(\theta_i,\phi_i)}{R_i^{n+1}}\right) \eta_n \langle r^n \rangle,$$

where the summation is over all considered point charges, R_i is the distance between the point charge and the Nd ion, and $\eta_n = \alpha_J/\beta_J/\gamma_J$ for n = 2/4/6. The Z_{nm}, $\alpha_J/\beta_J/\gamma_J$, and $\langle r^n \rangle$ are previously tabulated (*51*). After diagonalizing the Hamiltonian, we find that the Pr^{3+} $^3H_4$ 9-fold degeneracy and Nd^{3+} $^4I_{9/2}$ 10-fold degeneracy are split into 7 and 5 Stark levels, respectively. The resulting levels assuming a 3.33 Å *c*-lattice constant are listed in Table S1, with their numbering

in correspondence to Fig. 3 in the main text. In particular, the ground state of the split Pr^{3+} 4*f* levels is a singlet, as emphasized in the main text.

We can also calculate the easy axis anisotropy by examining $\langle g_J \mu_B J_{x/z} \rangle$ of the ground state levels in response to an external field along the *z*- or *x*-axis: $g_J \mu_B H_{x/z}$. Here g_J is the Landé g-factor, μ_B is the Bohr magneton and $J_{x/z}$ is the total angular momentum operator projection along the *x* or *z* axis. For both Pr- and Nd-nickelates, we find a larger response when field is applied in-plane as shown in fig. S7, indicating an easy-plane anisotropy. This is expected as the ground state of the split 4*f* levels has a dominant $|m = 0\rangle$ or $|m = \pm\frac{1}{2}\rangle$ component. The same crystal field splitting result can be obtained from symmetry arguments as well. For example, under a tetragonal symmetry, the Pr^{3+} 4*f* levels can be decomposed to 5 irreducible representations: A_{1g}, A_{2g}, B_{1g}, B_{2g}, E_g. They correspond to 5 nondegenerate energy levels and 2 doubly degenerate levels, consistent with previous reports (*53*) and our numerical calculation results.

Dependence of azimuthal angular magnetoresistance on measurement current direction

As discussed in the main text, the C_2 symmetric ϕ-dependent magnetoresistance seen in all nickelate samples can be attributed to vortex dynamics induced by the measurement current, while the C_4 symmetric response is attributed to the Nd 4*f* electrons in the underlying tetragonal crystal symmetry. Therefore, we expect the C_2 symmetric response to rotate with the current direction and the C_4 symmetric response to remain locked onto the crystalline axes. We perform such a test on a $Nd_{0.8}Sr_{0.2}NiO_2$ and a $Pr_{0.84}Sr_{0.16}NiO_2$ sample by sourcing current along the [110] direction. As shown in fig. S9, the clover leaf pattern of the Nd-nickelate sample retains the same orientation as

in Fig. 4, while the 'figure-of-eight'-shaped pattern of the Pr-nickelate sample is rotated by 45 degrees.

Broken symmetries in the Nd-nickelate's azimuthal angular magnetoresistance

In addition to the clear C_4 symmetric response in the Nd-nickelate's azimuthal angular magnetoresistance, signs of additional rotational and mirror symmetry breaking are observed. Fig. S10 shows in more detail the temperature and field dependence of the azimuthal angular magnetoresistance behavior plotted in Fig. S6, with a fixed measurement current of 10 μA. Here a clear C_2 symmetric feature is observed, which is qualitatively illustrated with a green shade in the leftmost panel. This feature exhibits sharp dips at ~32 degrees off of $\phi = 0/180$ axis and broad peaks around 135/315 degrees. This response is seen in multiple samples. Similar behavior in uncapped Nd-nickelate samples has been reported by three other groups (*46–48*), and interpreted as signs of nematicity. A satisfactory explanation would require experimental examination of potential lattice strain or structural distortion effects, and theoretical evaluation of the spontaneous symmetry breaking scenario. Additionally, Krieger et al. (*46*) investigated the effect of the capping layer in detail and found no qualitative dependence of the magnetoresistance on the capping layer.

Indications of Nd antiferromagnetic order

We find indirect evidence for antiferromagnetic order of the 4*f* moments in the doping evolution of the angular magnetoresistance measurements. Shown in fig. S11 are representative polar angle dependence data for $x = 0.15$, 0.175, 0.2 (sample #1), and 0.225 (sample #1) Sr doping at 2 K. A gradual but clear transition from an AOD dominant '∞'-shaped pattern to an EMP dominant 'figure-of-eight'-shaped pattern is seen as doping is increased. Such an enhancement of the

magnetic response of the 4*f* moments might seem counterintuitive, given the substitution of non-magnetic Sr^{2+} into the Nd^{3+} lattice. However, in the case of antiferromagnetism, non-magnetic defects can amplify the suppression of superconductivity by magnetic ordering (*39*), with the defects serving as effective magnetic scatterers due to the local imbalance between the up- and down-spin sublattice. In this sense, the observed doping dependence is consistent with antiferromagnetic ordering of the Nd 4*f* moments. Ultimately, a direct probe of Nd magnetism, although challenging for these thin films at very low temperatures, would be extremely insightful.

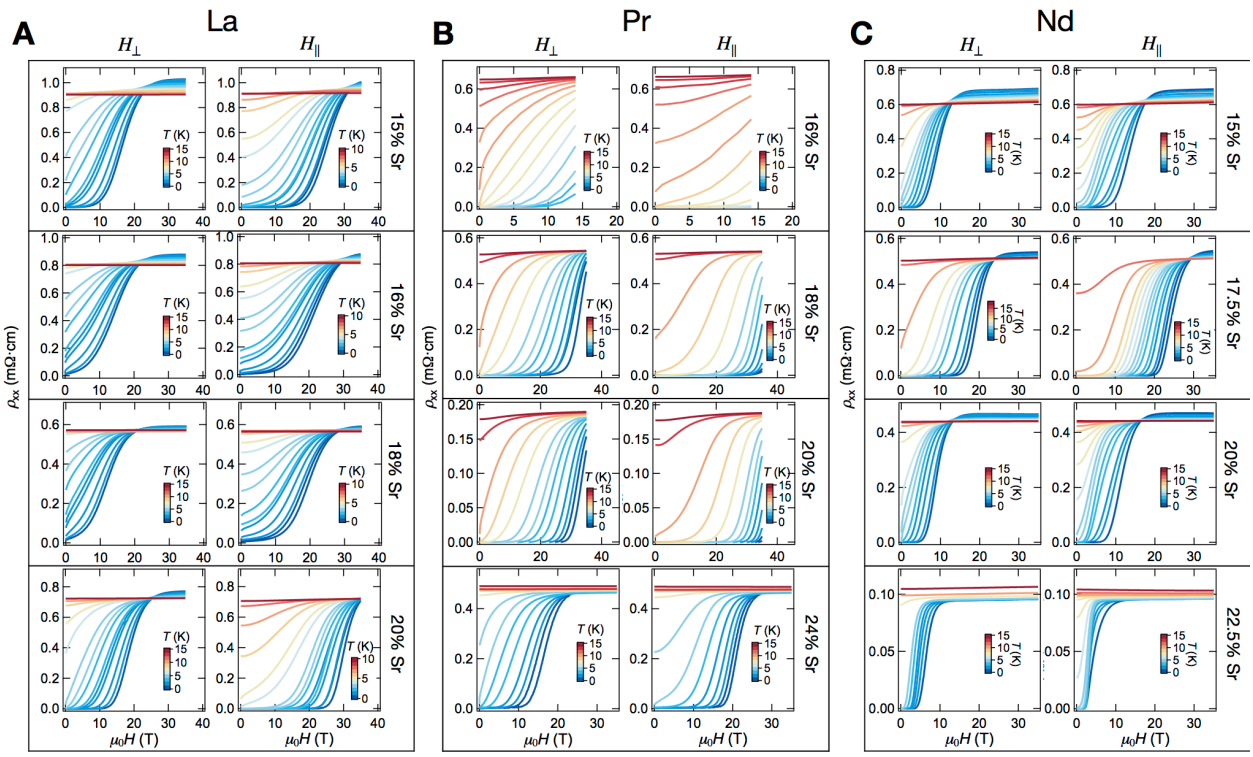

Fig. S1.

Doping dependence of the high field magnetoresistance in $R_{1-x}Sr_xNiO_2$. (**A - C**) Doping dependence of the $La_{1-x}Sr_xNiO_2$, $Pr_{1-x}Sr_xNiO_2$, and $Nd_{1-x}Sr_xNiO_2$ (*20*) magnetoresistance at temperatures ranging from 0.34 K to 18 K. For La-nickelates, x = 0.15, 0.16, 0.18, and 0.2; for Pr-nickelates, x = 0.16, 0.18, 0.2, and 0.24; and for Nd-nickelates, x = 0.15, 0.175, 0.2, and 0.225. The two columns of panels correspond to $H_\perp$ (left) and $H_\parallel$ (right) field orientations.

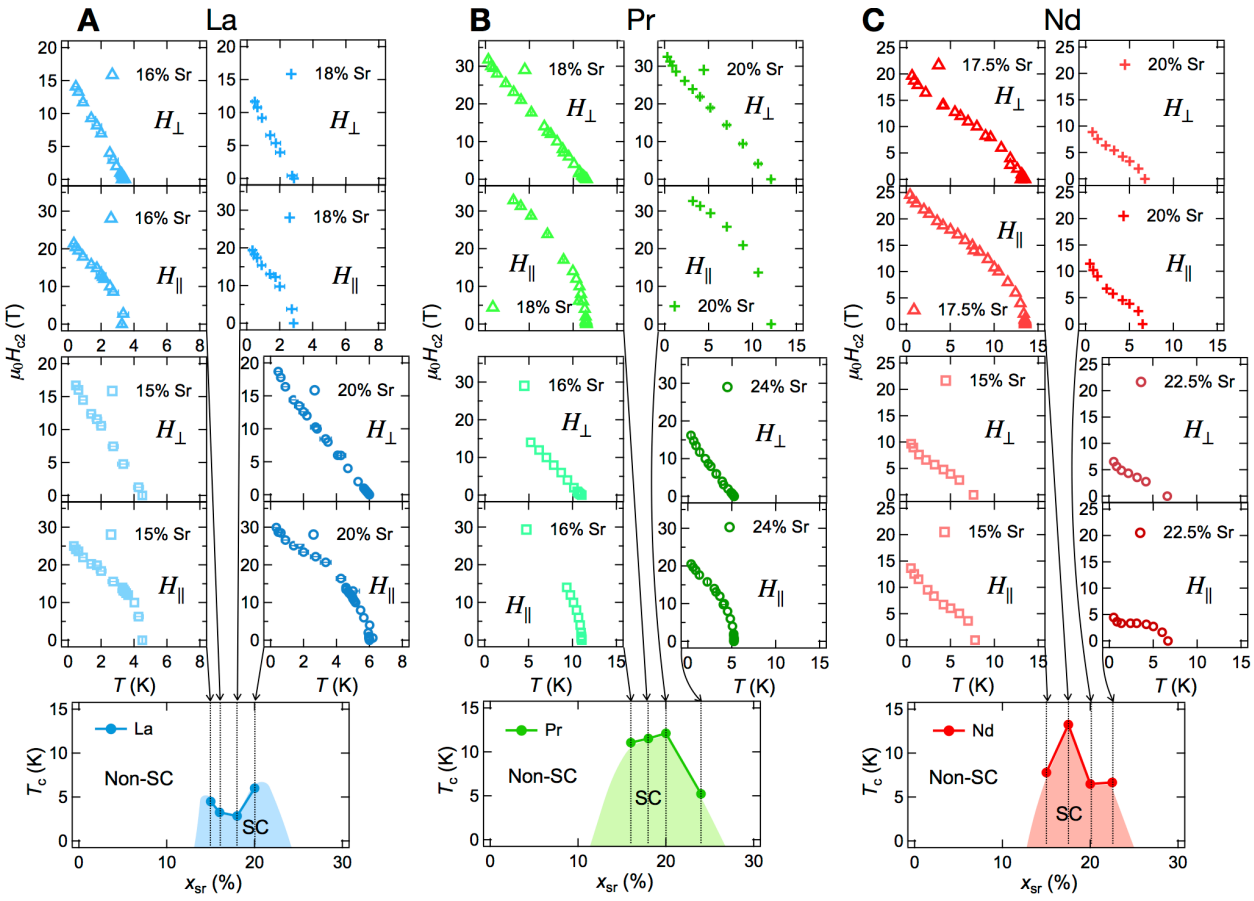

Fig. S2.

Doping dependence of H_{c2} in $R_{1-x}Sr_xNiO_2$. (**A - C**) $H_{c2}(T)$ data shown in fig. 1F of $La_{1-x}Sr_xNiO_2$, $Pr_{1-x}Sr_xNiO_2$, and $Nd_{1-x}Sr_xNiO_2$ (*20*). The doping of each pair is marked, by a black arrow, onto the corresponding superconducting domes shown in the three bottom panels.

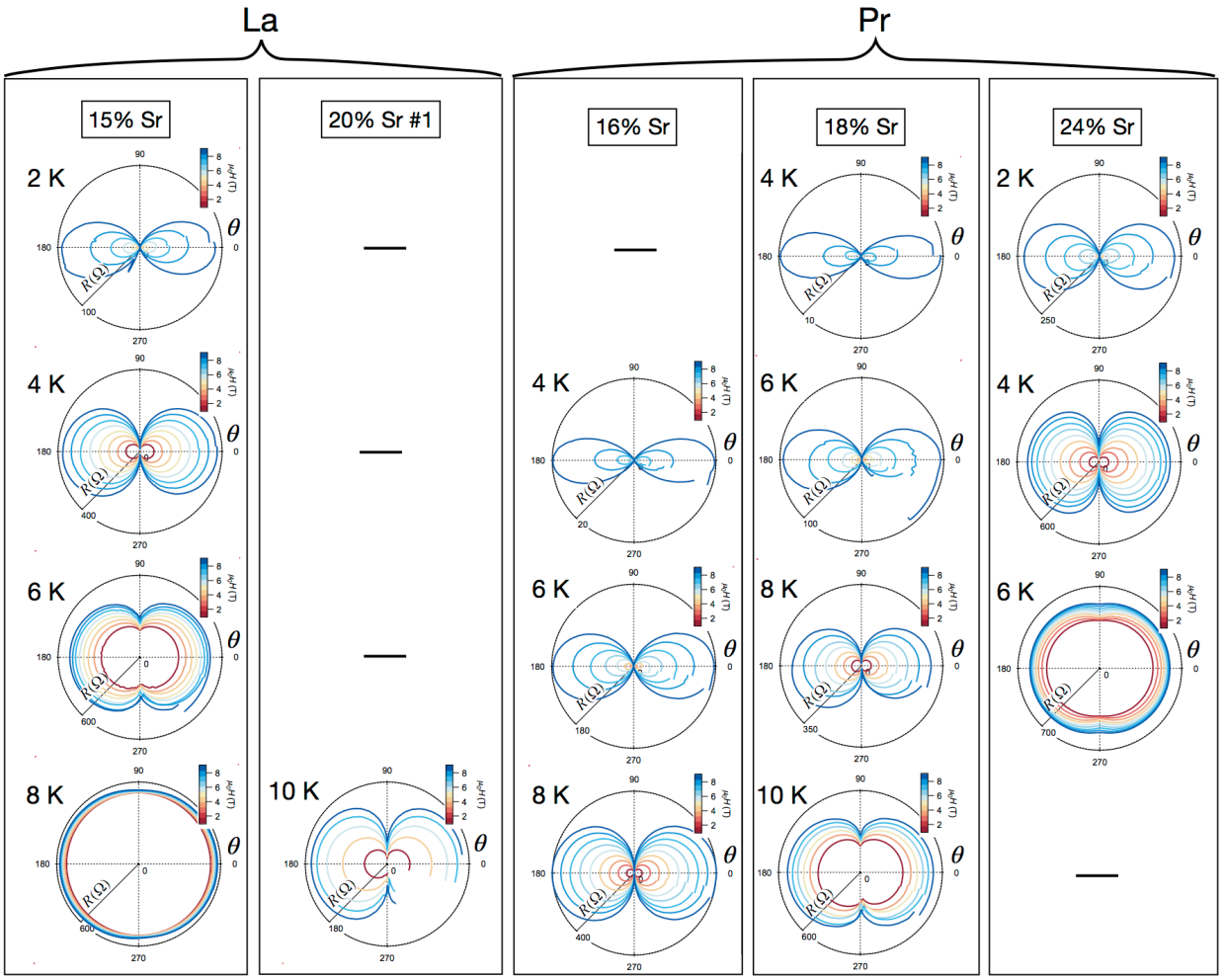

Fig. S3

Polar angular magnetoresistance of La- and Pr-nickelates. Temperature and magnetic field dependence of the polar angular magnetoresistance of $La_{1-x}Sr_xNiO_2$ for $x = 0.15$ and 0.2 and $Pr_{1-x}Sr_xNiO_2$ samples for $x = 0.16$, 0.18, and 0.24. Each column plots the data set of a separate sample. The different curves within each panel correspond to external field of 1 to 9 T (in 1 T increments), with larger resistance at larger field. The measurement temperature corresponding to each panel is shown in the top left corner.

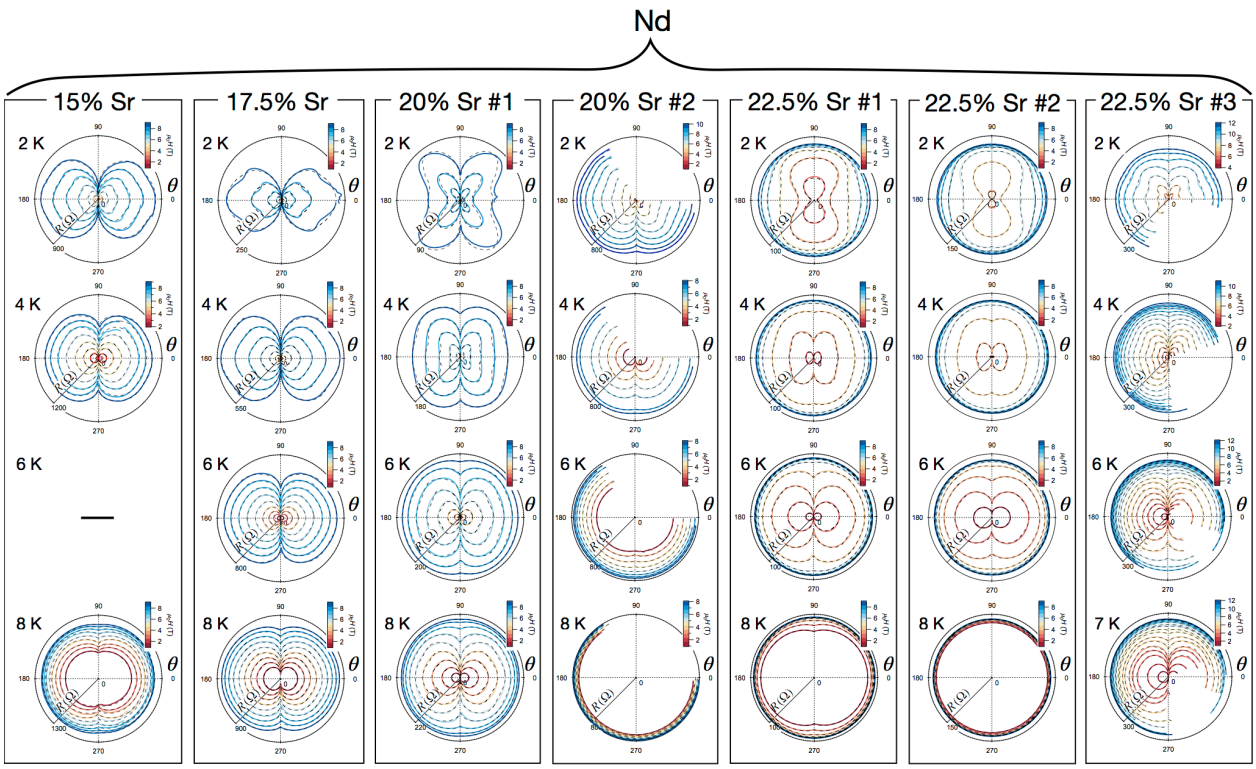

Fig. S4.

Doping dependence of the polar angular magnetoresistance in $Nd_{1-x}Sr_xNiO_2$. Doping dependence of the polar angular magnetoresistance at 2, 4, 6, 7 and 8 K for x = 0.15, 0.175, 0.2, and 0.225. Each column plots the data set of a separate sample. For x = 0.225, sample #1 corresponds to that in the main text Fig. 2 and 4. The different curves within each panel correspond to external field of 1 to 9 T, with larger resistance at larger field. The temperature corresponding to each panel is shown at its top left corner. Fits based on Eq. 1 in the main text are shown in black dashed lines.

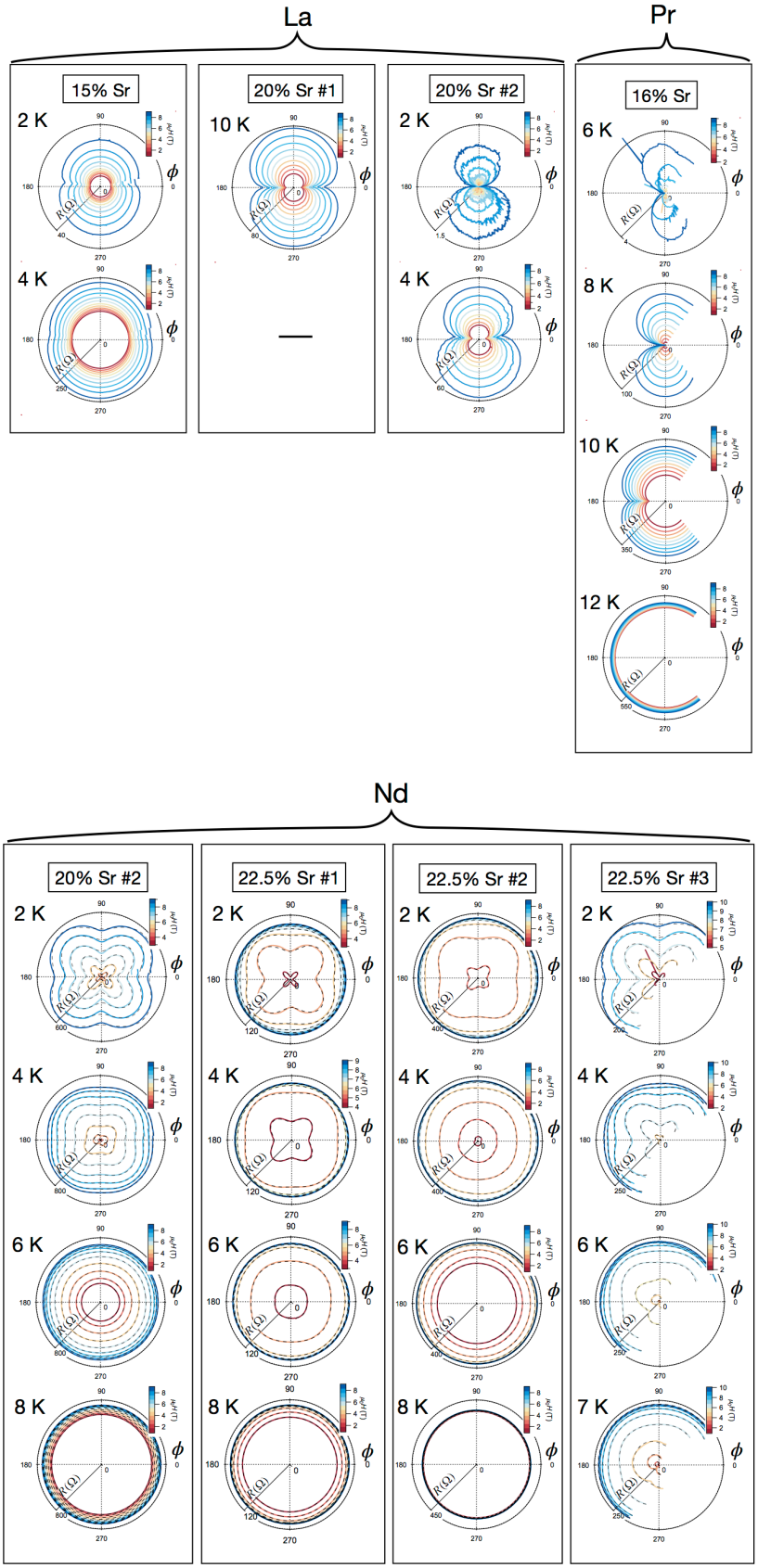
La
Pr
15% Sr
20% Sr #1
20% Sr #2
16% Sr
2 K
4 K
10 K
6 K
8 K
12 K
Nd
20% Sr #2
22.5% Sr #1
22.5% Sr #2
22.5% Sr #3
2 K
4 K
6 K
8 K
7 K

Fig. S5.

Azimuthal angular magnetoresistance of nickelates across A-site variants. Temperature and magnetic field dependence of polar angular magnetoresistance. Each column represents a separate sample. For $Nd_{0.775}Sr_{0.225}NiO_2$, the three samples correspond to those in fig. S4. Different curves within each panel correspond to external field of 1 to 9 T (in 1 T increments), with larger resistance at larger field. The temperature corresponding to each panel is shown at its top left corner. Fits to the Nd-nickelate data based on Eq. 2 in the main text are shown in black dashed lines.

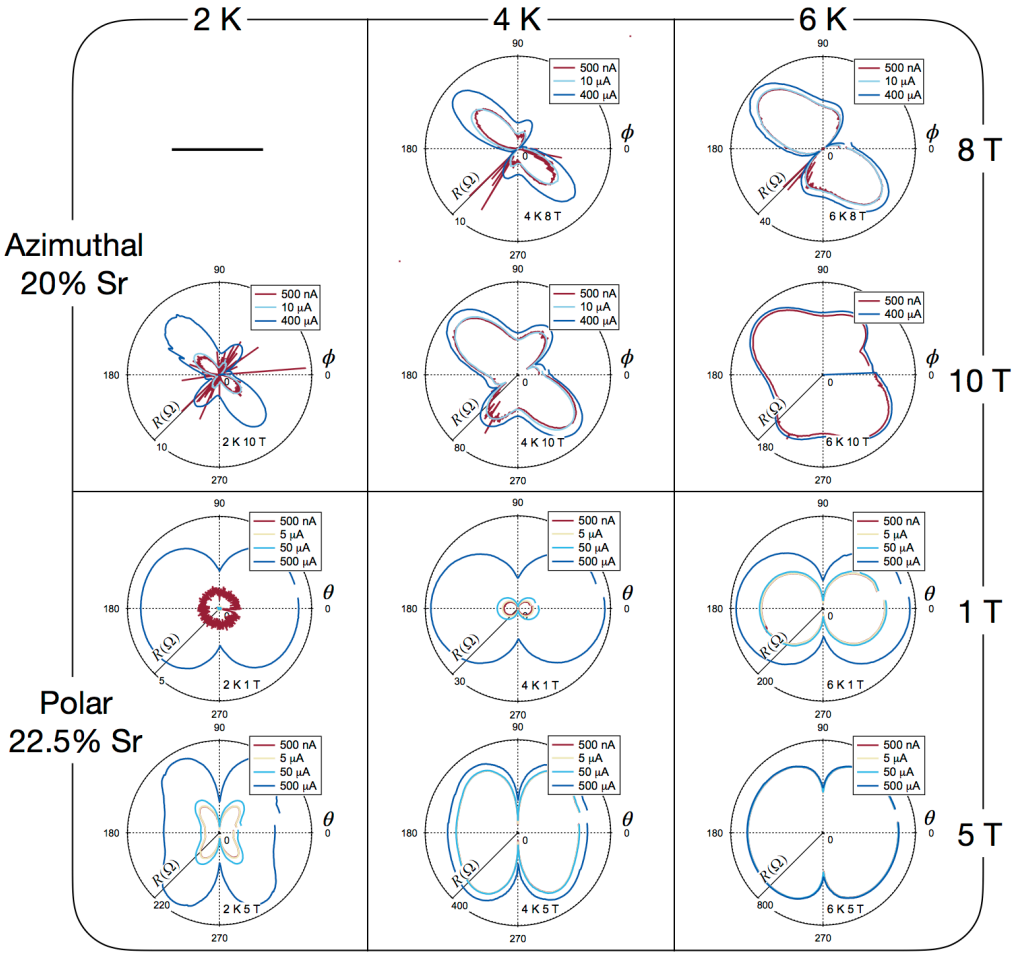

Fig. S6.

Current dependence of the anomalous angular magnetoresistance. Current dependence of the ϕ-dependent magnetoresistance of a $Nd_{0.8}Sr_{0.2}NiO_2$ sample at temperatures 2, 4, and 6 K and fields 8 and 10 T (upper panels), and the θ-dependent magnetoresistance of a $Nd_{0.775}Sr_{0.225}NiO_2$ sample at temperatures 2, 4, and 6 K and fields 1 and 5 T (lower panels). Different curves within each panel are associated with measurement currents ranging from 0.5 μA to 500 μA, corresponding to ~2 A/cm^2 to 2 kA/cm^2.

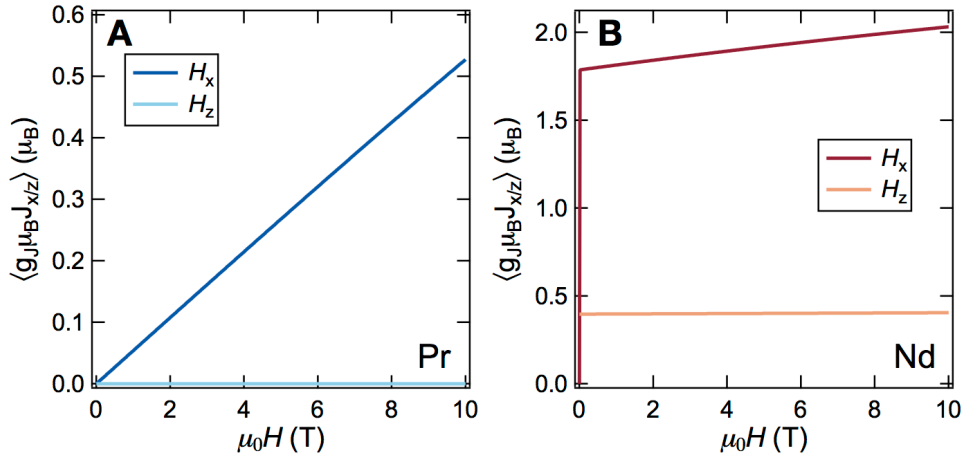

Fig. S7.

Calculated magnetic easy axis. (**A** and **B**) Effective magnetic moment of Pr^{3+} and Nd^{3+} in the presence of external in-plane and out-of-plane magnetic field for the ground state configuration.

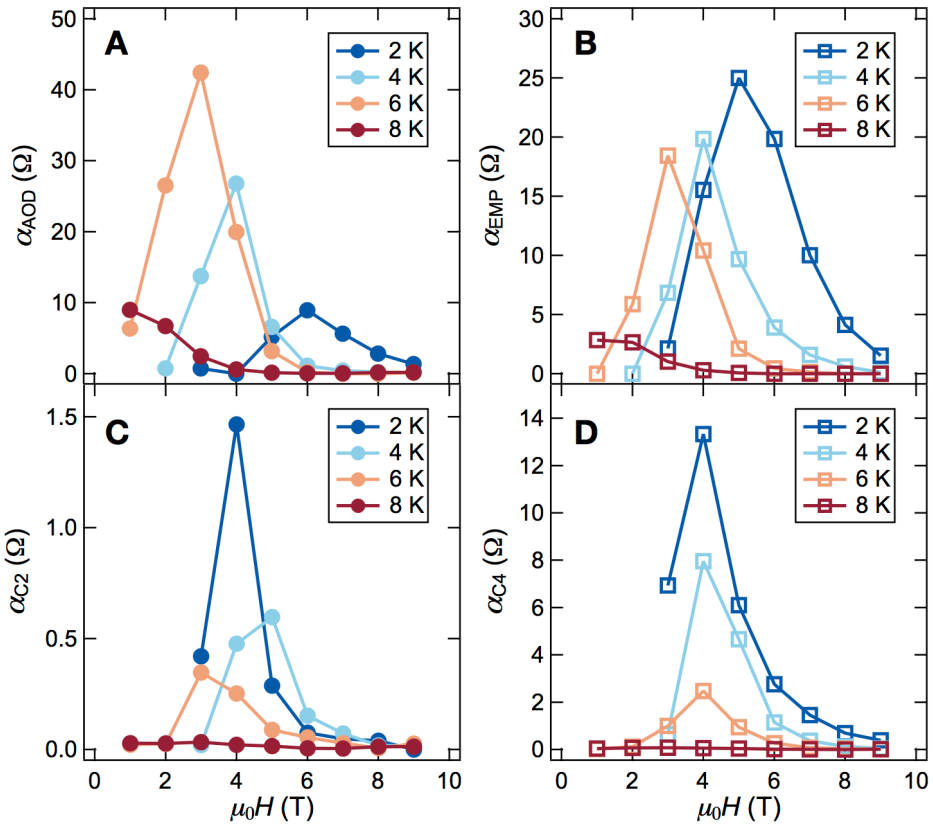

Fig. S8.

Temperature and field dependence of the fitting parameters. (**A** and **B**) Temperature and field dependence of the fit coefficients corresponding to the AOD and EMP terms in the polar angular dependence, respectively. (**C** and **D**) Temperature and field dependence of the fit coefficients corresponding to the C_2 and C_4 symmetric terms of the azimuthal angular dependence, respectively.

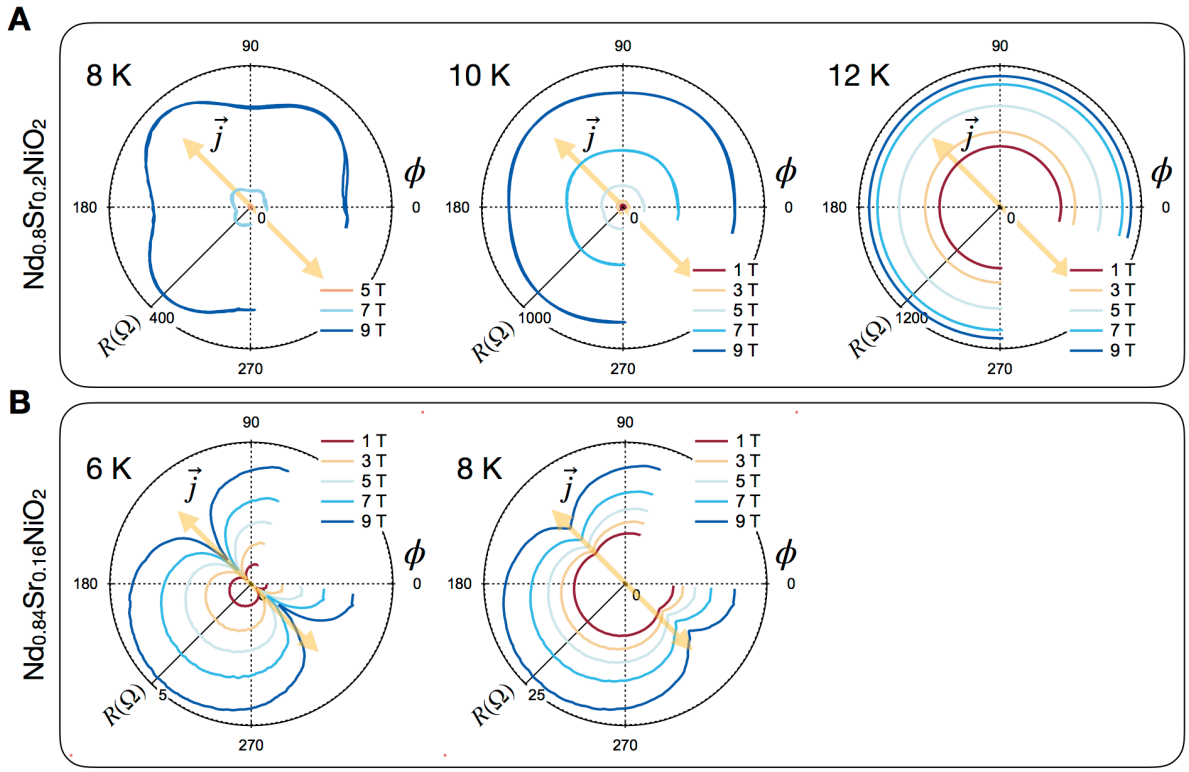

Fig. S9.

Current direction dependence of the ϕ-dependent magnetoresistance. (**A**) ϕ-dependent magnetoresistance of a $Nd_{0.8}Sr_{0.2}NiO_2$ sample at temperatures 8, 10, and 12 K and fields from 1 to 9 T. (**B**) ϕ-dependent magnetoresistance of a $Pr_{0.84}Sr_{0.16}NiO_2$ sample at temperatures 6 and 8 K and fields from 1 to 9 T. The direction of the measurement current is illustrated by the yellow arrow in both panels. For this specific measurement, $\phi = 0$ corresponds to the direction of the crystal *a*-axis.

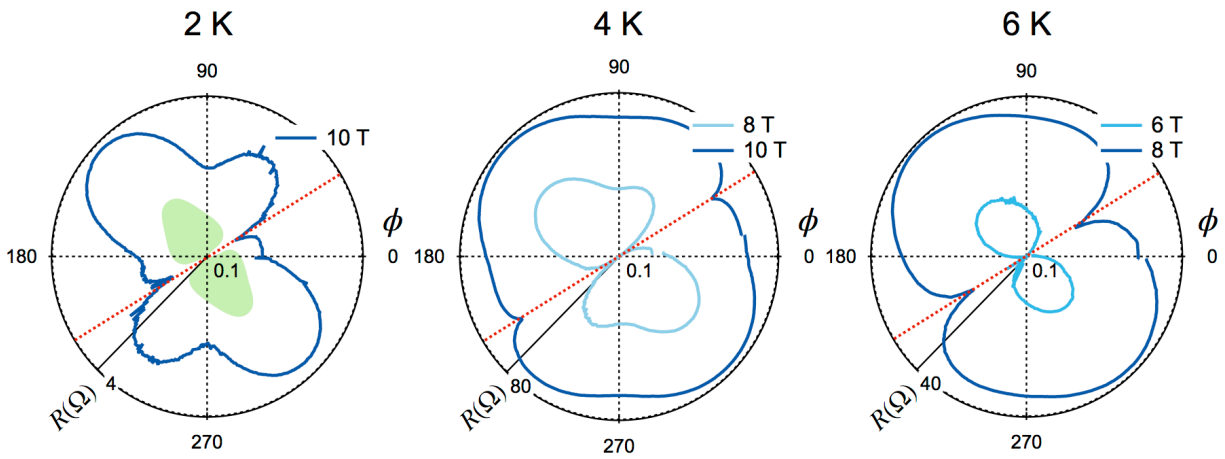

Fig. S10.

Additional broken symmetries in the azimuthal angular magnetoresistance. Temperature and field dependence of the ϕ-dependent magnetoresistance of the same sample shown in the top panel of Fig. S6. The measurement current is fixed at 10 μA and the radial axis of resistance is plotted on a log scale. The green shade illustrates the additional symmetry breaking C_2 response and the red dashed line marks the angular position of the sharp dips at $\phi \sim 32$ degrees.

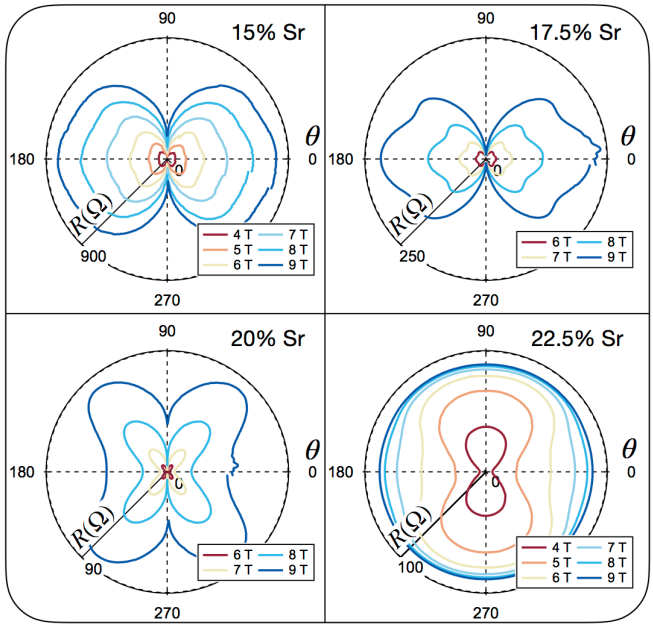

Fig. S11.

Indications of Nd 4*f* moment antiferromagnetic order in the doping dependence. Doping evolution of the (Nd,Sr)NiO_2 θ-dependent magnetoresistance at 2 K, with the doping level given at the top right corner of each panel.

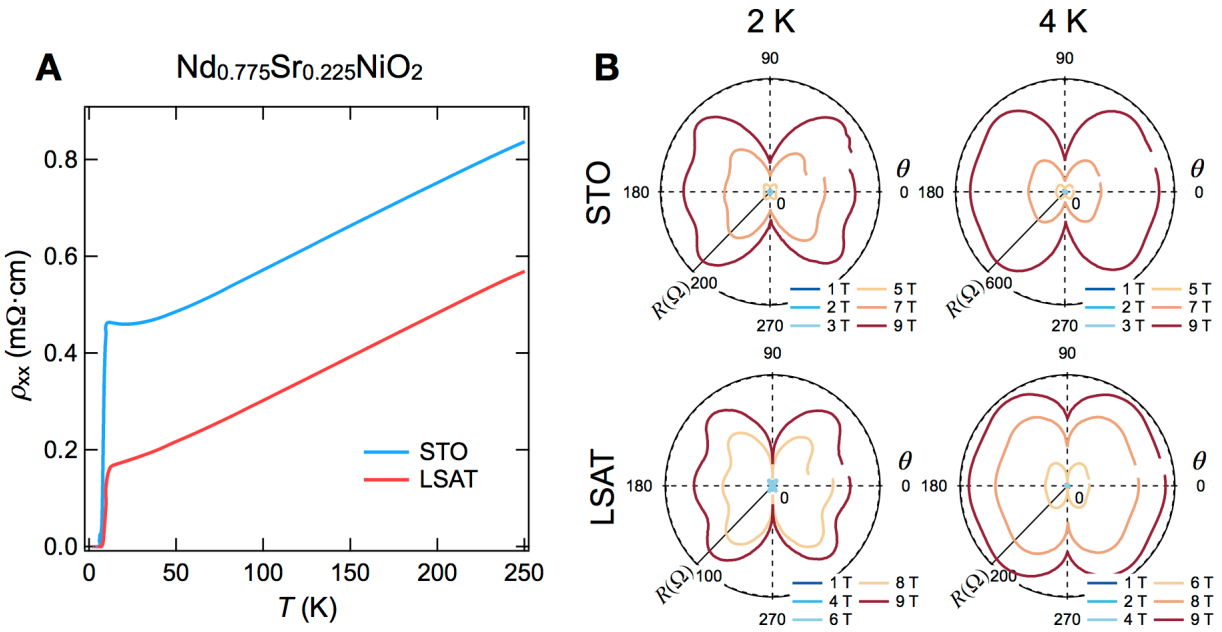

Fig. S12.

Independence of angular magnetoresistance on residual resistivity.

(**A**) Temperature dependent resistivity of two $Nd_{0.775}Sr_{0.225}NiO_2$ samples grown in previously reported conditions (*54*), with the legend specifying the corresponding substrate used. (**B**) Temperature and magnetic field dependent polar angular magnetoresistance of the two samples, with the substrate labeled on the left and measurement temperature labeled on the top.

Pr Levels	Pr $\|m\rangle$ Components	Nd Levels	Nd $\|m\rangle$ Components
L_0	$\|0\rangle$	L_0	$0.15\left\|\frac{9}{2}\right\rangle - 0.98\left\|\frac{1}{2}\right\rangle + 0.12\left\|-\frac{7}{2}\right\rangle$
L_1	$0.99\|1\rangle - 0.1\|-3\rangle$	L_1	$-0.15\left\|-\frac{9}{2}\right\rangle + 0.98\left\|-\frac{1}{2}\right\rangle - 0.12\left\|\frac{7}{2}\right\rangle$
L_2	$-0.99\|-1\rangle + 0.1\|3\rangle$	L_2	$-0.09\left\|\frac{5}{2}\right\rangle + 0.99\left\|-\frac{3}{2}\right\rangle$
L_3	$0.71\|2\rangle - 0.71\|-2\rangle$	L_3	$0.09\left\|-\frac{5}{2}\right\rangle - 0.99\left\|\frac{3}{2}\right\rangle$
L_4	$0.71\|2\rangle + 0.71\|-2\rangle$	L_4	$-0.09\left\|\frac{3}{2}\right\rangle - 0.99\left\|-\frac{5}{2}\right\rangle$
L_5	$0.73\|3\rangle - 0.07\|1\rangle + 0.07\|-1\rangle - 0.68\|-3\rangle$	L_5	$-0.99\left\|\frac{5}{2}\right\rangle - 0.09\left\|-\frac{3}{2}\right\rangle$
L_6	$-0.68\|3\rangle - 0.07\|1\rangle - 0.07\|-1\rangle - 0.73\|-3\rangle$	L_6	$-0.12\left\|\frac{9}{2}\right\rangle + 0.1\left\|\frac{1}{2}\right\rangle + 0.99\left\|-\frac{7}{2}\right\rangle$
L_7	$0.71\|4\rangle - 0.71\|-4\rangle$	L_7	$-0.12\left\|-\frac{9}{2}\right\rangle + 0.1\left\|-\frac{1}{2}\right\rangle + 0.99\left\|\frac{7}{2}\right\rangle$
L_8	$0.71\|4\rangle + 0.71\|-4\rangle$	L_8	$0.98\left\|-\frac{9}{2}\right\rangle + 0.16\left\|-\frac{1}{2}\right\rangle + 0.10\left\|\frac{7}{2}\right\rangle$
		L_9	$0.98\left\|\frac{9}{2}\right\rangle + 0.16\left\|\frac{1}{2}\right\rangle + 0.10\left\|-\frac{7}{2}\right\rangle$

Table S1.

CEF split 4*f* levels. Compositions of the 4*f* eigenstates under the tetragonal crystal field assuming a 3.33 Å *c*-lattice constant. Here $|m\rangle$ refers to the originally degenerate 4*f* atomic states, with *m* denoting the projected angular momentum quantum number. The L_x numberings correspond to Figs. 3, B and C in the main text.